ARTICLE

Quantitative Statistical Analysis of Dielectric Breakdown in Zirconia-Based Self-Assembled Nanodielectrics

Ruth A. Schlitz,[†,§] Young-geun Ha,[‡,⊥] Tobin J. Marks,[†,‡,*] and Lincoln J. Lauhon[†,*]

[†]Department of Materials Science & Engineering, Northwestern University, 2220 Campus Drive, Evanston, Illinois 60208, United States, and [‡]Department of Chemistry, Northwestern University, 2145 Sheridan Road, Evanston, Illinois 60208, United States. [§]Present address: Materials Research Laboratory, University of California, Santa Barbara, CA 93106, USA. [⊥]Present address: Nuclear Chemistry Research Division, Korea Atomic Energy Research Institute, Daeduk-Daero 989-111, Yuseong-gu, Daejeon, 305-353, Korea.

ABSTRACT

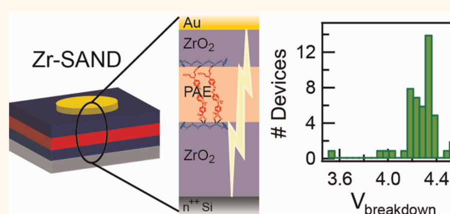

Uniformity of the dielectric breakdown voltage distribution for several thicknesses of a zirconia-based self-assembled nanodielectric was characterized using the Weibull distribution. Two regimes of breakdown behavior are observed: self-assembled multilayers >5 nm thick are well described by a single two-parameter Weibull distribution, with $\beta \approx 11$. Multilayers ≤5 nm thick exhibit kinks on the Weibull plot of dielectric breakdown voltage, suggesting that multiple characteristic mechanisms for dielectric breakdown are present. Both the degree of uniformity and the effective dielectric breakdown field are observed to be greater for one layer than for two layers of Zr-SAND, suggesting that this multilayer is more promising for device applications.

KEYWORDS: Weibull analysis · SAND · self-assembly · dielectric breakdown · reliability

Printed electronics offer the potential to dramatically lower the cost of moderate/large-area electronics by substituting low-cost roll-to-roll printing for expensive lithographic fabrication techniques.[1−6] At the heart of modern electronics is the field-effect transistor (FET); thus, the development of high-quality solution-processable materials for each component of an FET, *i.e.*, semiconductor channels,[1,5−11] metal interconnects,[4,5] and gate dielectrics,[5,6,10,12−14] is critical for the practical realization of this paradigm. While much research has been focused on developing solution-processed semiconductors, carrier mobilities in these materials (≤1 $cm^2/(V\ s)$) are typically much less than those of crystalline semiconductors (≥10^3 $m^2/(V\ s)$) in part due to the processing constraints (*e.g.*, temperatures <150 °C) necessary for compatibility with typical plastic substrates. Thus, in order to reduce operating voltages in printed transistors, development of high-capacitance solution-processed dielectrics is essential.

The key performance metric for an FET gate dielectric is how effectively it can modulate the carrier density at the semiconductor–dielectric interface. An intrinsic materials property that reflects the largest perturbation in carrier concentration possible for a given dielectric is the maximum electric displacement, D_{max}, which is defined as

$$D_{max} = \varepsilon_0 k E_{BD} \quad (1)$$

where ε_0 is the permittivity of free space, k is the dielectric constant, and E_{BD} is the dielectric breakdown field at which carriers are sufficiently energetic to cause irreversible damage to the dielectric by a mechanism such as breaking chemical bonds, thereby lowering the barrier to electron transport. Thus, device performance can be improved by either using a dielectric with a higher k or by improving the processing of the material to obtain higher quality microstructure with larger E_{BD}. Typical breakdown fields for both organic[15] and inorganic dielectrics for printed electronics are ≤10 MV/cm and are highly dependent on the processing conditions and the resultant impurity concentration and morphology of the dielectric. The mechanisms that cause dielectric breakdown fall into three general categories: electrical, where energetic carriers cause irreversible damage *via* a mechanism such as impact ionization;[15−17] thermal, where Joule heating from gate leakage current causes irreversible damage;[15] and in the case of mechanically compliant

* Address correspondence to t-marks@northwestern.edu; lauhon@northwestern.edu.

Received for review March 17, 2012 and accepted April 27, 2012.

Published online April 27, 2012
10.1021/nn3011834

© 2012 American Chemical Society

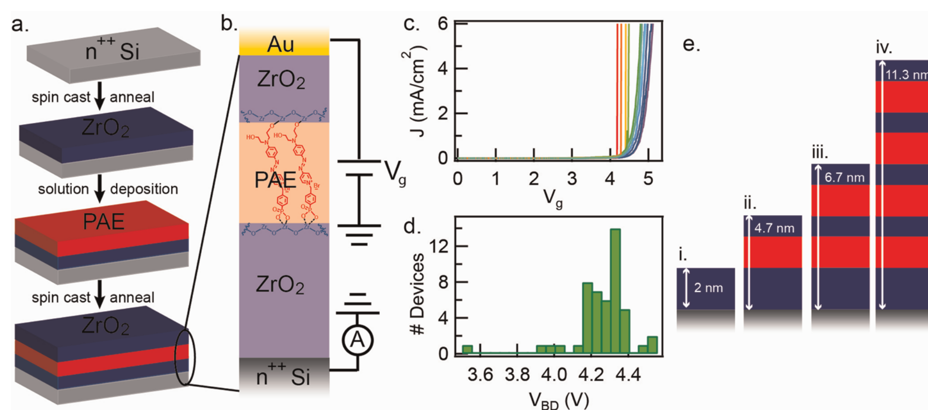

Figure 1. (a) Self-assembly procedure for iterative Zr-SAND film growth. Here PAE is the stilbazolium molecular layer shown in red. (b) Schematic of single-layer Zr-SAND metal−insulator−semiconductor capacitor and current−voltage measurement polarity. (c) Typical current density (J)−voltage (V_g) curves for 11 single-layer Zr-SAND MIS devices (sample 1L-500). (d) Histogram of extracted V_{BD} for the same sample of single-layer Zr-SAND (sample 1L-500), for comparison with its presentation as a Weibull plot in Figure 3 . (e) Relative physical thicknesses of (i) bare ZrO_2 primer layer, (ii) 1-layer, (iii) 2-layer, and (iv) 4-layer Zr-SAND.

materials such as polymers, electromechanical, where mechanical deformation due to the applied electric field contributes to breakdown.[15,18,19] Dielectric breakdown can also be caused by extrinsic flaws, including particulate contamination, pinholes in the dielectric, and local thickness variations. Inorganic dielectrics grown *via* conventional processes, SiO_2 in particular, have been well characterized both in the bulk and in thin films with thicknesses on the nanoscale.[16,17,20−22] However, the mechanisms responsible for breakdown in solution-processed dielectrics are not yet understood. In organics, the mechanisms for dielectric breakdown have been well characterized for some materials in bulk samples;[15] however, the mechanisms dominating dielectric breakdown in thin-film geometries are also not well understood. Understanding the mechanisms by which breakdown occurs in dielectrics for printable electronics would not only enable selection of the best candidate materials for device applications but also inform improvements in the composition and large-scale processing.

The other key figure of merit for gate dielectric performance in an FET is its specific capacitance, or capacitance per unit area, defined as

$$C_i = \varepsilon_0(k/d) \tag{2}$$

where d is the thickness of the dielectric. Thus, for a dielectric with a given k and at a given gate voltage, V_g, device performance will improve upon reduction of the dielectric thickness, d, subjecting the channel to a larger electric field. However, real dielectric materials have a finite resistance, and thus parasitic leakage currents traverse the dielectric under an applied electric field. As d is decreased to the nanoscale, the probability of electrons tunneling through the dielectric, and thus the parasitic leakage current density J_{leak}, increases exponentially. Quantum mechanical tunneling thus imposes a fundamental physical limit on the minimum practical physical thickness for a gate dielectric on the order of 1 nm. For this reason, the development of viable high-k dielectric materials, in addition to dielectrics with a high intrinsic E_{BD}, is essential for inorganic as well as organic or hybrid inorganic−organic gate dielectrics.

Self-assembled monolayers and multilayers are an emerging class of molecule-based dielectrics designed for flexible and transparent electronics.[5,10,12,23−30] Self-assembled nanodielectrics (SANDs),[10,14,29,31,32] in particular, are compelling due to their advantageous electronic properties including high capacitances,[29,31−33] low leakage current densities,[29,31,32,34,35] and the ability to form a high-quality electrical interface with a wide variety of channel materials.[29,33,36−40] In order for SANDs to successfully transition from a laboratory demonstration to a practical technology, they must exhibit a high degree of uniformity in their intrinsic electrical properties, in particular E_{BD}. For silane-based SAND materials, the dielectric breakdown voltage (V_{BD}) distribution has been shown previously to be highly uniform across many devices;[35] however, this high degree of uniformity requires both assembly under inert atmosphere and a relatively high-temperature (≥300 °C) annealing step that is not compatible with most plastic substrates useful for roll-to-roll printing.

Recently, a new type of SAND material, a zirconia-based multilayer SAND (Zr-SAND), has been developed for which self-assembly can be carried out in ambient[32] instead of previous vacuum[31] or inert atmosphere[29] methodologies, thus offering greater potential for large-scale application (Figure 1). These dielectrics have been characterized by a broad array of microstructural and electrical techniques and afford excellent thin-film transistor performance with a number of classes of organic and inorganic semiconductors.[32] Starting from this foundation, statistical evaluation of the distribution of dielectric breakdown voltages

becomes an essential step toward understanding the trade-offs between device reliability and capacitance for current and future SAND materials classes. Here we describe the measurement and Weibull analysis of the V_{BD} distribution for three thicknesses of Zr-SAND multilayers (1, 2, and 4 layers), as well as the bare ZrO_2 primer layer (Figure 1). We show that there are significant differences between multilayers $\leq$5 nm thick (bare ZrO_2, single-layer Zr-SAND) and >5 nm thick (2, 4 layers of Zr-SAND). Ultimately it will be seen that single-layer Zr-SAND offers the best trade-off between dielectric breakdown voltage magnitude, tightness of statistical distribution, capacitance, and leakage current density at a given electric field.

As shown in Figure 1, Zr-SAND is a structurally regular self-assembled multilayer consisting of solution-deposited ZrO_2 ($\sim$2 nm thick by X-ray reflectivity and TEM), followed by a self-assembled phosphonic acid-based stilbazolium π-electron precursor (PAE) monolayer ($\sim$1.5 nm thick by X-ray reflectivity and TEM) and another layer of ZrO_2 ($\sim$1 nm thick), thereby completing one layer of Zr-SAND (4.7 nm thick). Each PAE/ZrO_2 bilayer is $\sim$2.4 nm thick; subsequent ZrO_2/PAE bilayers can then be deposited in order to form the other materials studied: two layers (6.7 nm thick by X-ray reflectivity and TEM) and four layers (11.3 nm thick by X-ray reflectivity and TEM) of Zr-SAND (Figure 1e).

Dielectric breakdown is a stochastic process that is enabled by preferentially conductive defects or trap states randomly distributed throughout a dielectric.[41−43] Once any single conducting path, or short circuit, through the dielectric has been established, the entire device containing the dielectric undergoes failure. This type of failure is termed weakest-link failure in an analogy to mechanical failure of a linked chain.[43−45] Because this process is stochastic in nature, the measurement of many devices is essential to determine the nature of dielectric breakdown in a material and E_{BD}.

The statistical distribution that describes weakest-link failure is called the Weibull distribution. First popularized by Waloddi Weibull in 1951,[44] Weibull statistics are perhaps best known to materials chemists in the context of the brittle fracture of ceramics. In the context of dielectric breakdown, the Weibull distribution is typically employed to analyze time to breakdown, as it describes the lifetime of devices at a typical operating voltage. However, Zr-SAND is a new material, so obtaining information about the operational limits of this material for devices *via* a voltage to breakdown analysis is a necessary prerequisite to the more standard lifetime measurements intended to characterize the reliability of a dielectric over its operational lifetime. The voltage to breakdown distribution is also of Weibull form if a constant field ramp rate is employed, as is the case for our measurement procedure.[41,42] Note that in the present work, we primarily discuss dielectric breakdown voltage, V_{BD}, instead of breakdown field strength, E_{BD}. In a direct-current measurement, as is the case here, the individual layers of the Zr-SAND multilayer can be modeled as resistors in series, and thus the voltage drop across each is determined by the individual layer resistance. If the layer resistances are not uniform, the electric field will not be uniform. Since breakdown could be dependent on the current, voltage, or field within a particular layer of the dielectric, we cannot establish a unique breakdown field for these structures.

The two-parameter Weibull cumulative distribution function (CDF) is defined as

$$F(V_{BD}) = 1 - e^{-\left(\frac{V_{BD}}{\alpha}\right)^{\beta}} \quad (3)$$

where α, the scale parameter, is the voltage at which 63% of the devices have failed and β, the shape parameter, is the Weibull modulus that indicates the width of the distribution. Thus, a larger α indicates a larger breakdown strength, while a larger β indicates more uniformity in V_{BD} throughout the sample. To facilitate analysis, the Weibull CDF is often rearranged by taking two logarithms to produce a linear relationship,

$$\ln(-\ln(1 - F)) = \beta \ln(V_{BD}) - \beta \ln(\alpha) \quad (4)$$

so that the slope, β, and the *y*-intercept, $\beta \ln(\alpha)$, can easily be extracted from a plot of $\ln[-\ln(1 - F)]$ *versus* $\ln(V_{BD})$. This type of plot is called a Weibull plot, because data that are Weibull distributed will fall along a single line when plotted on these axes.

To acquire V_{BD} data, metal−insulator−semiconductor (MIS) parallel plate capacitors are first fabricated from cleaned n^{++} Si wafer substrates coated with various thicknesses of Zr-SAND and then a top Au electrode (30 nm thick). Three different thicknesses of Zr-SAND were used (1, 2, and 4 layers) as well as the bare sol−gel ZrO_2 primer layer alone (Figure 1; see Methods).[32] Au was deposited using a shadow mask with 200 μm, 500 μm, and 1 mm diameter circular cutouts. The resulting capacitors were approximately ellipsoidal in shape due to the angle of evaporation and the finite thickness of the shadow mask. Table 1 summarizes the devices studied.

Devices were contacted with flexible tungsten whisker probes, and current−voltage data were acquired in the geometry shown in Figure 1b and as described in the Methods. After measurement, each device was imaged with an optical microscope, and the capacitor area measured. Data from devices observed in the optical microscope to have large scratches from the tungsten whisker probe were excluded from analysis. The dielectric breakdown voltage, V_{BD}, was identified as the center of a 0.11 V range for which $dI/dV_g > 10^{-6}$ S. The V_{BD} criterion was chosen for two reasons: first, it is identical to that used in previous dielectric

TABLE 1. Characteristics Summary of Zr-SAND MIS Devices Studied

sample	# layers of Zr-SAND	thickness (nm)[32]	shadow mask diameter (μm)	average measured electrode area (cm^2)	
B-200	bare ZrO_2	2	200	1.53×10^{-4}	$\pm 1 \times 10^{-6}$
B-500	bare ZrO_2	2	500	15.55×10^{-4}	$\pm 2 \times 10^{-6}$
B-1000	bare ZrO_2	2	1000	71.0×10^{-4}	$\pm 1 \times 10^{-5}$
1L-200	1 layer	4.7	200	1.477×10^{-4}	$\pm 9 \times 10^{-7}$
1L-500	1 layer	4.7	500	15.33×10^{-4}	$\pm 4 \times 10^{-7}$
1L-1000	1 layer	4.7	1000	70.9×10^{-4}	$\pm 2 \times 10^{-5}$
2L-200	2 layers	6.7	200	1.69×10^{-4}	$\pm 2 \times 10^{-6}$
2L-500	2 layers	6.7	500	15.67×10^{-4}	$\pm 5 \times 10^{-6}$
2L-1000	2 layers	6.7	1000	70.6×10^{-4}	$\pm 2 \times 10^{-5}$
4L-200	4 layers	11.3	200	2.24×10^{-4}	$\pm 2 \times 10^{-6}$
4L-500	4 layers	11.3	500	17.38×10^{-4}	$\pm 5 \times 10^{-6}$
4L-1000	4 layers	11.3	1000	73.9×10^{-4}	$\pm 4 \times 10^{-5}$

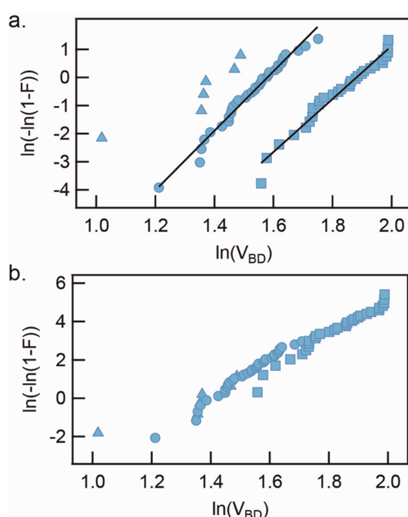

Figure 2. Weibull plots of 2-layer Zr-SAND V_{BD}. Data from three different sizes of MIS devices are shown: Samples 2L-1000 (triangles), 2L-500 (circles), 2L-200 (squares). (a) Linear fits used to extract Weibull parameters from the data are shown in black. (b) Data overlay on the Weibull plot after scaling to a common area of 1 mm^2, consistent with a random distribution of breakdown locations.

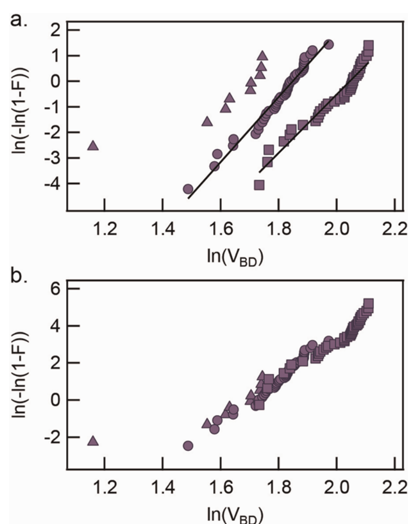

Figure 3. Weibull plots of 4-layer Zr-SAND V_{BD}. Data from three different sizes of MIS devices are shown: Samples 4L-1000 (triangles), 4L-500 (circles), and 4L-200 (squares). (a) Linear fits used to extract Weibull parameters from the data are shown in black. (b) Data overlay on the Weibull plot after scaling to a common area of 1 mm^2, consistent with a random distribution of breakdown locations.

breakdown voltage studies of a silane-based SAND,[35] and second, it correctly identifies abrupt breakdown events where there is a sudden increase in device conductivity. Furthermore, irreversible damage to Zr-SAND in the regime of the breakdown criterion was confirmed: devices were much more conductive at low voltages after dielectric breakdown had occurred. The V_{BD} data were plotted on a Weibull plot, and the Weibull parameters extracted *via* linear regression of the data. Extracted Weibull parameters were found to be insensitive to both the value and the type of breakdown criterion, as well as variations in capacitor area within each sample and the inclusion of data from scratched devices.[46]

RESULTS AND DISCUSSION

Multilayers >5 nm Thick: Weibull Analysis of 2- and 4-Layer Zr-SAND. Weibull plots for 2 and 4 layers of Zr-SAND are shown in Figures 2 and 3. The linear fit for each data set is displayed in black. A single line offers a good fit to the data, with an r^2 value of >0.95 for data sets with >30 V_{BD} data points (samples 2L-200, 2L-500, 4L-200, and 4L-500), indicating that the two- parameter Weibull distribution is a good description of the V_{BD} data. The extracted Weibull parameters for each data set are reported in Table 2. Deviations are within the 95% confidence bounds on the estimated rank and, thus, considered within the error of the fit. Data sets with <10 data points are not typically considered appropriate for Weibull analysis due to the large error bounds on the extracted Weibull parameters; however, it was not practical to measure a large number of the largest-area devices (2L-1000 and 4L-1000). Thus, we display the V_{BD} data for these samples alongside the larger data sets for comparison without performing a linear regression to fit to the Weibull distribution.

TABLE 2. Weibull Parameters Extracted for 2- and 4-Layer Zr-SAND

sample #	*n*	Weibull scale parameter α (V), 95% confidence range		Weibull shape parameter β, 95% confidence range		r^2
2L-200	30	6.6	[6.3 < α < 6.8]	9.4	[7.1 < β < 12.5]	0.97
2L-500	35	4.8	[4.7 < α < 5.0]	10.6	[8.3 < β < 13.5]	0.98
4L-200	40	7.7	[7.5 < α < 8.0]	11.4	[8.7 < β < 15.0]	0.95
4L-500	47	6.4	[6.2 < α < 6.5]	12.7	[10.1 < β < 16.0]	0.97

Fitting dielectric breakdown data to a Weibull distribution assumes that the breakdown locations are randomly distributed. If they are indeed random, the data will follow a scaling law[43] such that

$$\ln[-\ln(1-F_1)] - \ln[-\ln(1-F_2)] = \ln(A_1/A_2) \quad (5)$$

Thus, if breakdown is randomly distributed, data sets from different sized devices will have a statistically identical Weibull slope, β, and α will follow a similar scaling law, $V_{BD1}/V_{BD1} = [A_2/A_1]^{1/\beta}$.[43] To test this assumption, all of the data from for 2- and 4-layer Zr-SAND samples were scaled to a common area of 1 mm^2 using eq 5. Resultant Weibull plots are shown in Figures 2b and 3b, respectively. The data do indeed align, and area scaling is confirmed by the statistically identical β values for each distribution. The one exception is the single outlier from sample 4L-1000, which is located above the common line on the Weibull plot. Thus for this device, breakdown occurs at a lower voltage than predicted by the Weibull fit to the other data points. It is hypothesized that this device might have undergone dielectric breakdown by a different mechanism than the remaining devices. Ultimately, we find that the extracted V_{BD} for 165 of 166 devices analyzed are well fit by the Weibull distribution. Considering the statistical analysis, a Weibull slope of $\beta \approx 11$ describes both the 2- and 4-layer Zr-SAND. Area scaling is obeyed for each sample, implying that dielectric breakdown locations are randomly distributed.

Multilayers ≤5 nm Thick: Bare ZrO_2 and 1-Layer Zr-SAND. Thinner Zr-SAND multilayers are desirable due to their larger capacitances and smaller leakage current densities at a given field;[32] however, it will be seen that pinhole-type defects causing very low V_{BD} are more likely for bare ZrO_2 and single-layer Zr-SAND than for the multilayers >5 nm thick discussed above. Weibull analysis indicates a number of distinct breakdown modalities in the V_{BD} distribution, consistent with breakdown caused by multiple characteristic mechanisms.

Weibull plots containing V_{BD} data for bare ZrO_2 (samples B-200, B-500, B-1000) and 1-layer Zr-SAND (samples 1L-200, 1L-500, 1L-1000) are shown in Figures 4 and 5, respectively. Unlike the V_{BD} data for multiple layers of Zr-SAND presented above, the data are not convincingly fit by a single two-parameter Weibull distribution and do not fall on a single line when plotted on the Weibull plot. Upon further inspection,

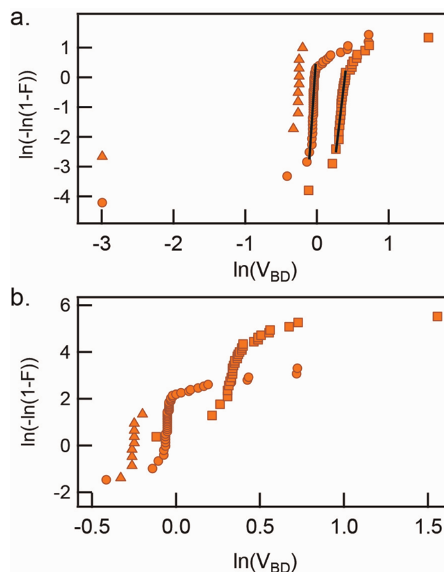

Figure 4. Weibull plots of the bare ZrO_2 primer layer. Data from three different sizes of MIS devices are shown: Samples B-1000 (triangles), B-500 (circles), B-200 (squares). (a) Linear fit for the voltage regime containing the majority of the data for each sample is displayed in black and was used to extract the Weibull parameters. (b) Weibull plot of bare ZrO_2 scaled to a common area of 1 mm, excluding very early V_{BD} points. Bare ZrO_2 does not follow area scaling, implying that breakdown is not randomly distributed.

however, multiple linear regions with distinct Weibull slopes can be identified. The linear region on the Weibull plot containing the majority of the data was fit to the two-parameter Weibull distribution; these fits are displayed as black lines in Figures 4a and 5a.

Data points that were not fit are typically rare events at either the high- or low-voltage tail of the V_{BD} distribution. The rare, early breakdown events are the most relevant for device applications, as it is these devices that will limit the operational range of devices on a chip. Inspection of the Weibull plot shows that these early breakdowns are overestimated by the Weibull distribution fit to the majority of the devices. Unlike the low-probability, low-V_{BD} tails on the data observed for silane-based SAND previously,[35] the present tails are all overestimated by the Weibull fit for the majority of the data and break down at lower voltages than would be predicted by fitting the majority of the data to a Weibull distribution. These tails suggest the presence of at least one distinct breakdown mechanism that dominates in this voltage range, but statistical analysis is precluded by the low number of data points.

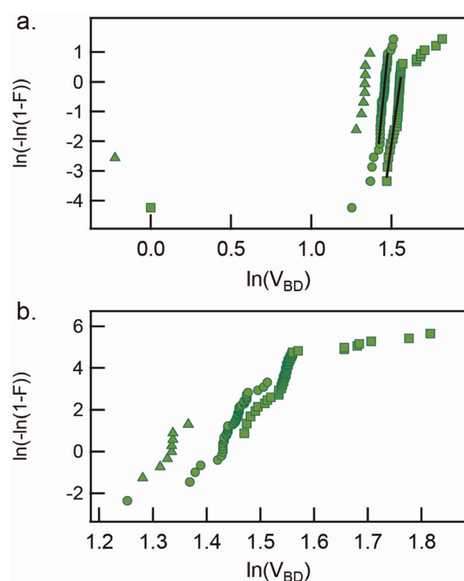

Figure 5. Weibull plot of 1-layer Zr-SAND. Data from three different sizes of MIS devices are shown: Samples 1L-1000 (triangles), 1L-500 (circles), and 1L-200 (squares). (a) The corresponding linear fits for the voltage regime containing the majority of the data are displayed in black and were used to extract the Weibull parameters reported. (b) Weibull plot of 1-layer Zr-SAND scaled to a common area of 1 mm^2 *via* eq 3, excluding the earliest V_{BD} data. The majority of the devices might appear to obey area scaling, but the kinks in the data do not align.

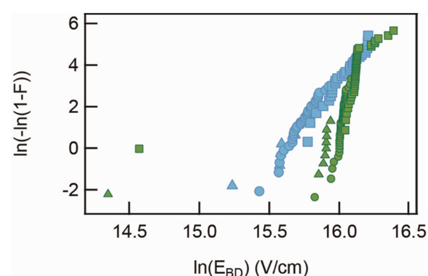

Figure 6. Weibull plot comparing effective breakdown fields, E_{BD}, for 1-layer and 2-layer Zr-SAND scaled to a common device area of 1 mm^2. Single-layer Zr-SAND data from samples 1L-1000 (triangles), 1L-500 (circles), and 1L-200 (squares) are shown in green, and data from 2-layer Zr-SAND data from samples 2L-1000 (triangles), 2L-500 (circles), and 2L-200 (squares) are shown in cyan. The distribution of E_{BD} is wider for 2-layer Zr-SAND, and earliest breakdowns occur at much lower fields.

For the majority of devices, the V_{BD} distributions for thin Zr-SAND and bare zirconia are tightly grouped, as indicated by the large Weibull slope, β. In fact, for many cases the breakdown events are so tightly grouped that multiple breakdown events are recorded as occurring at the same voltage. In this case, the finite step size for the voltage ramp ($\Delta V = 0.01$ V) was large enough that the detected V_{BD} values are binned in groups at 0.01 V intervals. Grouping leads to an artifact of infinite slope on the Weibull plot. The cumulative distribution function for grouped data was estimated by assuming that the largest breakdown in each group is equal to the measured V_{BD}. This method was used to calculate the Weibull parameters reported in Table 3. The Weibull plots shown in this section (Figures 4 and 5) include all V_{BD} data measured, including grouped data, and the fits shown are those to the estimated CDF. In general, the calculated Weibull parameters are statistically indistinguishable between the full CDF and the estimated CDF that accounts for grouped data; however, the goodness of fit as measured by the r^2 value is improved by eliminating the infinite slope artifacts that arise due to grouped data.

For the bare zirconia and 1-layer Zr-SAND data, kinks in the Weibull plots are observed, suggesting a multimodal V_{BD} distribution. Upon area scaling, as shown in Figures 4b and 5b, the kinks in the Weibull plot of the V_{BD} data do not align for either sample. If the kinks in the data were simply due to superposition of two-parameter Weibull distributions in V_{BD}, these kinks would be expected to align, as the voltage regime for which each mechanism dominates should be consistent for different electrode sizes. Reference to Figures 4b and 5b shows that this is not the case, and thus we conclude that breakdown is not randomly distributed in these samples. It is possible that some additional underlying variability in the Zr-SAND could cause this deviation from area scaling. For instance, small global variations in the bare zirconia primer thickness arising from spin coating could skew the distribution. A small, global thickness variation would be consistent with the area scaling observed for 2- and 4-layer Zr-SAND above, since such a variation would be less significant as a percentage of the overall dielectric thickness for the thicker multilayers. Nonetheless, area scaling demonstrates that a superposition of two-parameter Weibull distributions is insufficient to explain the V_{BD} behavior of bare zirconia and single-layer Zr-SAND, and a mechanism with a characteristic Weibull slope, β, cannot be assigned to a particular voltage range from this analysis. In summary, bare zirconia and single-layer Zr-SAND Weibull plots exhibit

TABLE 3. Summary of Weibull Parameters for Bare Zirconia and 1-Layer Zr-SAND

sample[a]	n	scale parameter α (V), 95% confidence range		shape parameter β, 95% confidence range		r^2
B-200	20	1.47	[$1.37 < \alpha < 1.59$]	20	[$8 < \beta < 53$]	0.97
B-500	32	0.97	[$0.94 < \alpha < 1.0$]	38	[$18 < \beta < 80$]	0.92
1L-200	39	4.7	[$4.6 < \alpha < 4.9$]	38	[$18 < \beta < 77$]	0.94
1L-500	41	4.30	[$4.26 < \alpha < 4.34$]	55	[$37 < \beta < 81$]	0.97

[a] Data were grouped, and uncertainty bounds calculated ignoring censored data, as described in the Methods.

clear kinks in the Weibull plots, reflecting a multimodal V_{BD} distribution and suggesting the presence of multiple characteristic mechanisms for dielectric breakdown for low and high V_{BD}.

CONCLUSIONS

The Zr-SAND multilayers exhibit two differing regimes of Zr-SAND dielectric breakdown voltage behavior: 2- and 4-layer Zr-SAND multilayers are well-described by the two-parameter Weibull distribution, while single-layer Zr-SAND and bare zirconia exhibit multimodal V_{BD} distributions with a few very early breakdowns. By comparing these two characteristic types of breakdown behavior, we can use the statistical information to identify which multilayer synthesized *via* the current process is most promising for practical application. As discussed above, for transistor performance, the critical parameter is not V_{BD}, but instead the effective breakdown field, E_{BD}. To estimate E_{BD} for Zr-SAND, the V_{BD} was divided by the Zr-SAND thickness values from Table 1. The E_{BD} distribution for thin and thick Zr-SAND multilayers can then be compared by plotting them together on a single Weibull plot: Figure 6 shows the E_{BD} distribution for 1- and 2-layer Zr-SAND (plotted in green and cyan, respectively) scaled to a common 1 mm^2 area to rule out systematic differences in device size across different samples. Inspection of the plot shows that the overall E_{BD} distribution for 2-layer Zr-SAND is broader than that for single-layer Zr-SAND and that E_{BD} is systematically smaller for 2-layer Zr-SAND, with the exception of the very rare, very low-voltage breakdowns discussed above for single-layer Zr-SAND. We conclude that the addition of the second layer of Zr-SAND (2.5 nm thick) creates additional pathways for electronic transport and dielectric breakdown, perhaps by disturbing the existing single-layer Zr-SAND. This behavior is consistent with previously reported leakage current behavior for Zr-SAND. At an applied field of 2 MV/cm, J_{leak} for single-layer Zr-SAND was reported to be only 7×10^{-8} A/cm^2, while adding a second layer of Zr-SAND increases the leakage current density to 2×10^{-7} A/cm^2.[32] Note that both of these leakage current densities are smaller than that previously reported for sol–gel processed ZrO_2 alone, implying that the presence of the molecular PAE layer is beneficial and significantly reduces the leakage current density.[47] Furthermore, the morphology of single-layer Zr-SAND has previously been observed to be more uniform than that for 2-layer Zr-SAND: AFM images reveal that single-layer Zr-SAND has a smaller rms roughness than 2-layer Zr-SAND.[32] The observation in the literature of both reversible leakage currents and morphological uniformity is consistent with both the E_{BD} magnitude and Weibull modulus described in this work.

Because the rare, very early breakdown events observed in single-layer Zr-SAND are likely due to a particular type of defect, such as a pinhole through the dielectric or a particulate contaminant, process optimization, such as fabrication in a cleanroom-type environment, offers potential to significantly reduce the population of devices with very low V_{BD}. If, after process optimization, these devices are sufficiently robust, single-layer Zr-SANDs will clearly be the best candidate Zr-SAND for practical FET application. Of the Zr-SANDs studied here, single-layer Zr-SAND has the highest capacitance, the tightest V_{BD} distribution, and a systematically larger E_{BD} for the majority of devices. Furthermore, single-layer Zr-SAND exhibits a larger E_{BD} and lower leakage current densities than sol–gel processed ZrO_2 alone. Excluding the rare, early breakdowns, typical E_{BD} values for 1-layer Zr-SAND, are larger than those for 2-layer Zr-SAND, indicating that an additional multilayer might in fact be detrimental to the dielectric strength of the material. While we do not rule out the potential for optimization of Zr-SAND multilayer self-assembly to mitigate the detrimental effects of depositing a second layer, ultimately, of the materials studied, the single-layer Zr-SAND combines high capacitance, low rms roughness, a high Weibull slope, β, and a typical V_{BD} comparable to thicker Zr-SAND multilayers.

In conclusion, the V_{BD} distribution for Zr-SAND multilayers >5 nm thick is well described by a Weibull distribution, as is the case for conventional dielectric materials such as SiO_2. Furthermore, Weibull analysis is shown to be useful to establish the presence of multiple breakdown mechanisms active in differing gate voltage regimes. This analysis points the way for control studies that can isolate the mechanisms in question through modification of dielectric chemistry and processing. It is clear from the presence of rare, very low E_{BD} devices that average properties and small sample sizes are insufficient to evaluate candidate dielectric materials for practical application. Weibull analysis is clearly a valuable tool to understand and evaluate unconventional molecular dielectrics for device applications.

METHODS

Zr-SAND samples were prepared on n^{++} Si wafer substrates according to the previously reported process.[32] For the initial ZrO_2 primer layer (~2 nm thick), the silicon substrate is spin-coated with zirconium precursor solution and then cured at 150 °C to drive off solvent and prepare it for self-assembly of the PAE layer (~1.5 nm thick). The PAE is solution-deposited by immersing the substrate in a solution of the precursor for 30 min at 60 °C. Another layer of ZrO_2 is then spin-coated and cured at 150 °C, completing the first Zr-SAND layer (~2.4 nm on top of the primer). Subsequent ZrO_2/PAE bilayers are deposited by repeating the spin-coat and solution deposition steps.

Zr-SAND MIS parallel-plate capacitors were fabricated in a process identical to that used in previous studies of silane-based SAND[29] electronic transport mechanisms[34] and dielectric breakdown statistics.[35] A shadow mask was gently placed on top of a freshly grown SAND sample, with care taken to avoid mechanical abrasion by sliding the shadow mask along the surface, and secured with rare-earth magnets. The shadow mask consisted of three sizes of circular windows with diameters of 200 μm, 500 μm, and 1 mm, respectively. The evaporation chamber was evacuated to a pressure of $\sim 10^{-6}$ Torr prior to deposition. Slow deposition rates were used to minimize any damage to the Zr-SAND: the first 10 nm was evaporated slowly at a rate of ~0.02 Å/s, and then the rate was increased to ~0.3 Å/s for the remaining material (~30 nm total thickness). Due to the angle of evaporation and the finite thickness of the shadow mask, the resulting capacitors were approximately ellipsoidal in shape.

The Zr-SAND samples were prepared for measurement using a diamond scribe to scrape through the Zr-SAND in order to electrically contact the degenerately doped Si substrate with a probe tip. The samples were then exposed to a pressurized N_2 stream to remove particulates generated during the scraping process and were then placed directly in a vacuum probe station (MMR). A home-built aluminum stage held the sample, and a glass microscope slide was used to electrically isolate the sample from the stage. The chamber remained at room temperature and was pumped down to a pressure of $\sim 10^{-5}$ Torr prior to and during the measurement, which was carried out in the dark. A flexible tungsten whisker probe, 1 μm in diameter at the tip (Signatone model SE-SM), was used to make electrical contact with the gold top electrode in order to minimize mechanical damage to the Zr-SAND. Voltage was applied to the top Au electrode while the Si substrate was kept at ground potential, per Figure 1a. The signal from the grounded probe was fed into a current preamplifier and then to an analog to digital converter. Thus, when a positive voltage was applied to the Au, the n^{++} substrate was in accumulation; current−voltage curves for statistical analysis were performed in positive polarity only.

The voltage was ramped slowly and at a constant rate, ~0.01 V/s, with a voltage step size of 0.01 V. Then, 500 current measurements were acquired and averaged for each 0.01 V step; the delay prior to each acquisition was 500 ms. When either the current reached a magnitude of 1×10^{-5} A or the Au electrode began to degrade, the measurement was stopped. Electrode degradation was inferred when large fluctuations in the measured current were detected at current magnitudes of ~1 μA. Degradation was confirmed *via* both postmeasurement inspection in the optical microscope and separate observations of three devices in real time. All devices were inspected after measurement in an optical microscope. Device areas were calculated from the acquired images using a script in ImageJ, and data from devices with significant scrapes from the tungsten probe tip were noted and excluded from further analysis.

Measured current−voltage ($I-V$) curves were analyzed in IGOR to extract a dielectric breakdown voltage for each device. V_{BD} was identified as the lowest voltage at which $dI/dV \geq 1\ \mu$S at the center of a 0.11 V range. In other words, V_{BD} was identified as the lowest voltage at which the 10 surrounding data points (five higher and five lower) meet or exceed the breakdown criterion when fit to a line. This procedure was implemented using IGOR. Irreversible changes to the Zr-SAND devices in the regime of the threshold were confirmed in two ways, either through measurement of a second $I-V$ curve after the initial measurement or by observation of the top electrode degrading.

Data were fit to the Weibull distribution using a Weibull plot constructed from the V_{BD} data. Median ranks were estimated with the inverse of the F distribution *via* the following equation:

$$w_a(x_i) = \frac{1}{\frac{n-i+1}{i}(F_{1-\alpha,\,2(n-i+1),\,2i}+1)} \tag{6}$$

where $w_a(x_i)$ is the $100(1-\alpha)$ nonparametric confidence limit ($\alpha = 0.5$ for median rank), i is the order in which the device failed (*i.e.*, first, second, third, *etc.*), n is the total number of data points, and $F_{1-\alpha,2(n-i+1),2i}$ is the critical value from the F distribution.[48,49] These ranks were used to generate a Weibull plot, and the Weibull parameters were estimated *via* linear regression of the data. Maximum likelihood confidence bounds on the Weibull parameters were estimated *via* the local information matrix, otherwise known as the Fisher matrix.[48,49]

The procedure to fit multiple Weibull slopes and excluded outliers was as follows: a Weibull plot was generated for the entire data set, and then linear regression was performed on the subranges of the data that are of interest. Confidence bounds were calculated *via* a Fisher matrix, with all data not included in a particular linear fit included in the calculation of the information matrix as censored data.[48,49] If this calculation resulted in the generation of imaginary confidence bounds, the calculation was then performed without the censored data points. If this further calculation still results in the generation of imaginary confidence bounds, this is noted and bounds were not reported. Confidence bounds on the subpopulations of the data were not calculated.

Conflict of Interest: The authors declare no competing financial interest.

Acknowledgment. This work was supported by the MRSEC program of the National Science Foundation (DMR-1121262 and DMR-0520513) at the Northwestern University Materials Research Center and by AFOSR under contract FA9550-08-1-0331. We thank M. Ratner and K. Faber for helpful discussions.

REFERENCES AND NOTES

1. Bao, Z.; Rogers, J. A.; Katz, H. E. Printable Organic and Polymeric Semiconducting Materials and Devices. *J. Mater. Chem.* **1999**, *9*, 1895–1904.
2. Rogers, J. A.; Someya, T.; Huang, Y. Materials and Mechanics for Stretchable Electronics. *Science* **2010**, *327*, 1603–1607.
3. Sirringhaus, H. Device Physics of Solution-Processed Organic Field-Effect Transistors. *Adv. Mater.* **2005**, *17*, 2411–2425.
4. Perelaer, J.; Smith, P. J.; Mager, D.; Soltman, D.; Subramanian, V.; Korvink, J. G.; Schubert, U. S. Printed Electronics: the Challenges Involved in Printing Devices, Interconnects, and Contacts Based on Inorganic Materials. *J. Mater. Chem.* **2010**, *20*, 8446–8453.
5. Sun, J.; Zhang, B.; Katz, H. E. Materials for Printable, Transparent, and Low-Voltage Transistors. *Adv. Funct. Mater.* **2011**, *21*, 29–45.
6. Kjellander, B. K. C.; Smaal, W. T. T.; Anthony, J. E.; Gelinck, G. H. Inkjet Printing of TIPS-PEN on Soluble Polymer Insulating Films: A Route to High-Performance Thin-Film Transistors. *Adv. Mater.* **2010**, *22*, 4612–4616.
7. Dimitrakopoulos, C. D.; Malenfant, P. R. L. Organic Thin Film Transistors for Large Area Electronics. *Adv. Mater.* **2002**, *14*, 99–117.
8. Murphy, A. R.; Fréchet, J. M. J. Organic Semiconducting Oligomers for Use in Thin Film Transistors. *Chem. Rev.* **2007**, *107*, 1066–1096.
9. Wen, Y.; Liu, Y. Recent Progress in n-Channel Organic Thin-Film Transistors. *Adv. Mater.* **2010**, *22*, 1331–1345.
10. Marks, T. J. Materials for Organic and Hybrid Inorganic/Organic Electronics. *MRS Bull.* **2010**, *35*, 1018–1027.
11. Liu, C.; Minari, T.; Lu, X.; Kumatani, A.; Takimiya, K.; Tsukagoshi, K. Solution-Processable Organic Single Crystals with Bandlike Transport in Field-Effect Transistors. *Adv. Mater.* **2011**, *23*, 523–526.
12. DiBenedetto, S. A.; Facchetti, A.; Ratner, M. A.; Marks, T. J. Molecular Self-Assembled Monolayers and Multilayers for Organic and Unconventional Inorganic Thin-Film Transistor Applications. *Adv. Mater.* **2009**, *21*, 1407–1433.
13. Facchetti, A.; Yoon, M.-H.; Marks, T. J. Gate Dielectrics for Organic Field-Effect Transistors: New Opportunities for Organic Electronics. *Adv. Mater.* **2005**, *17*, 1705–1725.
14. Ortiz, R. P.; Facchetti, A.; Marks, T. J. High-k Organic, Inorganic, and Hybrid Dielectrics for Low-Voltage Organic Field-Effect Transistors. *Chem. Rev.* **2010**, *110*, 205–239.

15. Ieda, M. Dielectric Breakdown Process of Polymers. *IEEE Trans. Electr. Insul.* **1980**, *EI-15*, 206–224.
16. Degraeve, R.; Groeseneken, G.; Bellens, R.; Ogier, J. L.; Depas, M.; Roussel, P. J.; Maes, H. E. New Insights in the Relation Between Electron Trap Generation and the Statistical Properties of Oxide Breakdown. *IEEE Trans. Electron Devices* **1998**, *45*, 904–911.
17. Stathis, J. H. Percolation Models for Gate Oxide Breakdown. *J. Appl. Phys.* **1999**, *86*, 5757.
18. Stark, K. H.; Garton, C. G. Electric Strength of Irradiated Polythene. *Nature* **1955**, *176*, 1225–1226.
19. Neff, H. F.; Lima, A. M. N.; Melcher, E. U. K.; Moreira, C. S.; Barreto Neto, A. G. S.; Precker, J. W. An Electro-thermal Approach to Dielectric Breakdown in Solids: Application to Crystalline Polymer Insulators. *IEEE Trans. Dielectr. Electr. Insul.* **2010**, *17*, 872–880.
20. Apte, P. P.; Saraswat, K. C. Correlation of Trap Generation to Charge-to-Breakdown (Q_{bd}): a Physical-Damage Model of Dielectric Breakdown. *IEEE Trans. Electron Devices* **1994**, *41*, 1595–1602.
21. Dumin, D. J.; Maddux, J. R.; Scott, R. S.; Subramoniam, R. A Model Relating Wearout to Breakdown in Thin Oxides. *IEEE Trans. Electron Devices* **1994**, *41*, 1570–1580.
22. Wu, E. Y.; Sune, J.; Lai, W. On the Weibull Shape Factor of Intrinsic Breakdown of Dielectric Films and its Accurate Experimental Determination. Part II: Experimental Results and the Effects of Stress Conditions. *IEEE Trans. Electron Devices* **2002**, *49*, 2141–2150.
23. Acton, O.; Ting, G.; Ma, H.; Ka, J. W.; Yip, H.-L.; Tucker, N. M.; Jen, A. K.-Y. π-σ-Phosphonic Acid Organic Monolayer/Sol–Gel Hafnium Oxide Hybrid Dielectrics for Low-Voltage Organic Transistors. *Adv. Mater.* **2008**, *20*, 3697–3701.
24. Aswal, D. K.; Lenfant, S.; Guerin, D.; Yakhmi, J. V.; Vuillaume, D. Self Assembled Monolayers on Silicon for Molecular Electronics. *Anal. Chim. Acta* **2006**, *568*, 84–108.
25. Collet, J.; Vuillaume, D. Nano-Field Effect Transistor with an Organic Self-Assembled Monolayer as Gate Insulator. *Appl. Phys. Lett.* **1998**, *73*, 2681–2683.
26. Fontaine, P.; Goguenheim, D.; Deresmes, D.; Vuillaume, D.; Garet, M.; Rondelez, F. Octadecyltrichlorosilane Monolayers as Ultrathin Gate Insulating Films in Metal-Insulator-Semiconductor Devices. *Appl. Phys. Lett.* **1993**, *62*, 2256–2258.
27. Halik, M.; Klauk, H.; Zschieschang, U.; Schmid, G.; Dehm, C.; Schutz, M.; Maisch, S.; Effenberger, F.; Brunnbauer, M.; Stellacci, F. Low-Voltage Organic Transistors with an Amorphous Molecular Gate Dielectric. *Nature* **2004**, *431*, 963–966.
28. Ma, H.; Acton, O.; Ting, G.; Ka, J. W.; Yip, H.-L.; Tucker, N.; Schofield, R.; Jen, A. K.-Y. Low-Voltage Organic Thin-Film Transistors with π-σ-Phosphonic Acid Molecular Dielectric Monolayers. *Appl. Phys. Lett.* **2008**, *92*, 113303.
29. Yoon, M.-H.; Facchetti, A.; Tobin, J. Marks σ-π Molecular Dielectric Multilayers for Low-Voltage Organic Thin-Film Transistors. *Proc. Natl. Acad. Sci. U. S. A.* **2005**, *102*, 4678–4682.
30. Park, Y. D.; Kim, D. H.; Jang, Y.; Hwang, M.; Lim, J. A.; Cho, K. Low-Voltage Polymer Thin-Film Transistors with a Self-Assembled Monolayer as the Gate Dielectric. *Appl. Phys. Lett.* **2005**, *87*, 243509.
31. DiBenedetto, S. A.; Frattarelli, D. L.; Facchetti, A.; Ratner, M. A.; Marks, T. J. Structure–Performance Correlations in Vapor Phase Deposited Self-Assembled Nanodielectrics for Organic Field-Effect Transistors. *J. Am. Chem. Soc.* **2009**, *131*, 11080–11090.
32. Ha, Y.-G.; Emery, J. D.; Bedzyk, M. J.; Usta, H.; Facchetti, A.; Marks, T. J. Solution-Deposited Organic–Inorganic Hybrid Multilayer Gate Dielectrics. Design, Synthesis, Microstructures, and Electrical Properties with Thin-Film Transistors. *J. Am. Chem. Soc.* **2011**, *133*, 10239–10250.
33. Byrne, P. D.; Facchetti, A.; Marks, T. J. High-Performance Thin-Film Transistors from Solution-Processed Cadmium Selenide and a Self-Assembled Multilayer Gate Dielectric. *Adv. Mater.* **2008**, *20*, 2319–2324.
34. DiBenedetto, S. A.; Facchetti, A.; Ratner, M. A.; Marks, T. J. Charge Conduction and Breakdown Mechanisms in Self-Assembled Nanodielectrics. *J. Am. Chem. Soc.* **2009**, *131*, 7158–7168.
35. Schlitz, R. A.; Yoon, K. H.; Fredin, L. A.; Ha, Y.-G.; Ratner, M. A.; Marks, T. J.; Lauhon, L. J. Weibull Analysis of Dielectric Breakdown in a Self-Assembled Nanodielectric for Organic Transistors. *J. Phys. Chem. Lett.* **2010**, *1*, 3292–3297.
36. Hur, S.-H.; Yoon, M.-H.; Gaur, A.; Shim, M.; Facchetti, A.; Marks, T. J.; Rogers, J. A. Organic Nanodielectrics for Low Voltage Carbon Nanotube Thin Film Transistors and Complementary Logic Gates. *J. Am. Chem. Soc.* **2005**, *127*, 13808–13809.
37. Ju, S.; Kim, S.; Mohammadi, S.; Janes, D. B.; Ha, Y.-G.; Facceti, A.; Marks, T. J. Interface Studies of ZnO Nanowire Transistors Using Low-Frequency Noise and Temperature-Dependent I-V Measurements. *Appl. Phys. Lett.* **2008**, *92*, 022104.
38. Chen, P.-C.; Shen, G.; Chen, H.; Ha, Y.-G.; Wu, C.; Sukcharoenchoke, S.; Fu, Y.; Liu, J.; Facchetti, A.; Marks, T. J.; *et al.* High-Performance Single-Crystalline Arsenic-Doped Indium Oxide Nanowires for Transparent Thin-Film Transistors and Active Matrix Organic Light-Emitting Diode Displays. *ACS Nano* **2009**, *3*, 3383–3390.
39. Kim, H. S.; Byrne, P. D.; Facchetti, A.; Marks, T. J. High Performance Solution-Processed Indium Oxide Thin-Film Transistors. *J. Am. Chem. Soc.* **2008**, *130*, 12580–12581.
40. Kim, H.-S.; Won, S. M.; Ha, Y.-G.; Ahn, J.-H.; Faccheti, A.; Marks, T. J.; Rogers, J. A. Self-Assembled Nanodielectrics and Silicon Nanomembranes for Low Voltage, Flexible Transistors, and Logic Gates on Plastic Substrates. *Appl. Phys. Lett.* **2009**, *95*, 183504.
41. Hill, R. M.; Dissado, L. A. Theoretical Basis for the Statistics of Dielectric Breakdown. *J. Phys. C: Solid State* **1983**, *16*, 2145–2156.
42. Dissado, L. A.; Fothergill, J. C.; Wolfe, S. V.; Hill, R. M. Weibull Statistics in Dielectric Breakdown; Theoretical Basis, Applications and Implications. *IEEE Trans. Electr. Insul.* **1984**, *EI-19*, 227–233.
43. Wu, E. Y.; Vollertsen, R.-P. On the Weibull Shape Factor of Intrinsic Breakdown of Dielectric Films and its Accurate Experimental Determination. Part I: Theory, Methodology, Experimental Techniques. *IEEE Trans. Electron Devices* **2002**, *49*, 2131–2140.
44. Weibull, W. A Statistical Distribution Function of Wide Applicability. *J. Appl. Mech.* **1951**, *18*, 293–297.
45. Le, J.-L.; Bažant, Z. P.; Bazant, M. Z. Lifetime of High-k Gate Dielectrics and Analogy with Strength of Quasibrittle Structures. *J. Appl. Phys.* **2009**, *106*, 104119.
46. Schlitz, R. A. Characterizing Electronic Inhomogeneities of Nanoscale Materials for Printable Electronics. Ph.D. Dissertation, Northwestern University, Evanston, IL, 2012.
47. Ha, Y.; Jeong, S.; Wu, J.; Kim, M.-G.; Dravid, V. P.; Facchetti, A.; Marks, T. J. Flexible Low-Voltage Organic Thin-Film Transistors Enabled by Low-Temperature, Ambient Solution-Processable Inorganic/Organic Hybrid Gate Dielectrics. *J. Am. Chem. Soc.* **2010**, *132*, 17426–17434.
48. Dodson, B. *Weibull Analysis*; ASQC Quality Press: Milwaukee, WI, 1994.
49. Dodson, B. *The Weibull Analysis Handbook*; ASQ Quality Press: Milwaukee, WI, 2006.